Probabilistic Near-Field Tsunami Source and Tsunami Run-up Distribution Inferred From Tsunami Run-up Records in Northern Chile

Jun-Whan Lee[1] , **Jennifer L. Irish[1,2]** , and **Robert Weiss[2,3]**

[1]Department of Civil and Environmental Engineering, Virginia Tech, Blacksburg, VA, USA, [2]Center for Coastal Studies, Virginia Tech, Blacksburg, VA, USA, [3]Department of Geosciences, Virginia Tech, Blacksburg, VA, USA

Abstract Understanding a tsunami source and its impact is vital to assess a tsunami hazard. Thanks to the efforts of the tsunami survey teams, high-quality tsunami run-up data exist for contemporary events. Still, it has not been widely used to infer a tsunami source and its impact mainly due to the computational burden of the tsunami forward model. In this study, we propose a TRRF-INV (Tsunami Run-up Response Function-based INVersion) model that can provide probabilistic estimates of a near-field tsunami source and tsunami run-up distribution from a small number of run-up records. We tested the TRRF-INV model with synthetic tsunami scenarios in northern Chile and applied it to the 2014 Iquique, Chile, tsunami event as a case study. The results demonstrated that the TRRF-INV model can provide a reasonable tsunami source estimate to first order and estimate tsunami run-up distribution well. Moreover, the case-study results agree well with the United States Geological Survey report and the global Centroid Moment Tensor solution. We also analyzed the performance of the TRRF-INV model depending on the number and the uncertainty of run-up records. We believe that the TRRF-INV model has the potential for supporting accurate hazard assessment by (1) providing new insights from tsunami run-up records into the tsunami source and its impact, (2) using the TRRF-INV model as a tool to support existing tsunami inversion models, and (3) estimating a tsunami source and its impact for ancient events where no data other than estimated run-up from sediment deposit data exist.

Plain Language Summary Thanks to tsunami survey teams, there are observations of the highest elevation flooded by tsunamis in discrete locations. However, these data have not been widely used to determine where the earthquake that triggered the tsunami occurred, how large the earthquake was, and how large and extensive the floods caused by the tsunami were. In this study, we develop a new computer model that can identify the earthquake information and the flooding extent along the coastline from the discrete flood observations. The new computer model is tested for thousands of artificial earthquake scenarios and a historical earthquake event that occurred in 2014 in Chile. The results show that the new computer model can estimate the earthquake information and the flooding extent well. We believe that this new computer model can advance understanding of historical tsunami events and lead to better preparedness plans for possible future tsunamis.

1. Introduction

Tsunamis, mainly caused by shallow subduction-zone earthquakes, can cause severe damage to coastal communities once they occur, especially to near-field areas. To mitigate the tsunami damage and increase the resiliency of coastal communities, it is crucial to better understand a tsunami source and assess its impact. To better understand the tsunami source, tsunami inversion models, which can infer a tsunami source from observed data, have been widely developed (Satake, 2009). Depending on the input data, tsunami inversion models can be divided into three types. The first type is a tsunami inversion model that relies on seismic waveform data alone or combined with other data such as local strong motion, GPS (Global Positioning System), InSAR (Interferometric Synthetic Aperture Radar), and DART (Deep-ocean Assessment and Reporting of Tsunamis) data (e.g., Lay et al., 2011; Yokota et al., 2011; Yue et al., 2014). Instead of relying on seismic waveform data, the second type is a tsunami inversion model that uses tsunami waveforms (such as DART, tide gauge data) alone or combined with GPS and/or InSAR data (e.g., Ho et al., 2019; Romano et al., 2016; Williamson et al., 2017; Zhou et al., 2019). This methodology was first proposed by

Satake (1987) and is receiving increased attention, especially after the *Mw* 9.0 2011 Tohoku-Oki earthquake, because one of the main reasons for enormous casualties and tsunami damage is known to be due to underestimating the earthquake's magnitude and resulting tsunami run-up by relying on the early arrival of seismic waveform data alone (Hoshiba & Ozaki, 2014). The third type is a tsunami inversion model that uses tsunami sediment deposit data to infer the historical tsunami source, especially for the paleotsunami events (e.g., Ioki & Tanioka, 2016; MacInnes et al., 2010; Martin et al., 2008; Nanayama et al., 2003). Once a tsunami source is estimated, a tsunami forward model – usually a high-fidelity physics-based numerical model that can simulate tsunami propagation and inundation processes from a given tsunami source – is then used to assess the impact of tsunamis.

A tsunami run-up, the maximum ground elevation wetted by the tsunami, is one of the important characteristics to quantify the impact of a tsunami. Thanks to the tsunami survey teams such as the International Tsunami Survey Team (ITST), there are many high-quality tsunami run-up data sets for contemporary events (e.g., Arcos et al., 2019; Synolakis & Okal, 2005). For this reason, the tsunami run-up distribution along the coastline is usually employed to validate the tsunami source and to evaluate the impact of tsunamis. However, there are only a few studies that directly used tsunami run-up data to infer a tsunami source (e.g., Fuentes et al., 2016; MacInnes et al., 2010; Piatanesi et al., 1996). One of the main reasons is the tsunami forward model's computational burden because a tsunami inversion model requires a large number of tsunami forward simulations to find a tsunami source that best matches the tsunami run-up records. Even though several tsunami forward models employed computational techniques to improve the computational efficiency, such as adaptive mesh refinement and parallelization techniques (e.g., Mandli et al., 2016; Popinet, 2015), estimating a tsunami run-up distribution using high-fidelity physics-based numerical models remains computationally intensive. For this reason, Fuentes et al. (2016) and Piatanesi et al. (1996) have relied on a less accurate but faster tsunami forward model than the high-fidelity model, which estimates run-up by multiplying an amplification factor and the maximum wave height of the offshore point, to consider a large number of scenarios. On the other hand, MacInnes et al. (2010) used a high-fidelity tsunami forward model but considered only a handful of scenarios determined by expert judgment.

To overcome the computational burden of the high-fidelity physics-based numerical model, Lee et al. (2020) recently developed a tsunami forward model based on a response surface methodology, hereafter Tsunami Run-up Response Function (TRRF) model that can rapidly estimate a near-field tsunami run-up distribution over real topography without substantial loss of accuracy, with respect to high-fidelity models. The main concept of the TRRF model is that the tsunami run-up distribution can be decomposed into (1) a leading-order contribution being modeled by fault parameters using the Okal and Synolakis (2004)'s empirical formula and (2) a regional component that is dictated by the local topography.

This study proposes a new tsunami inversion model based on the TRRF model to infer a near-field tsunami source and tsunami run-up distribution from tsunami run-up records: hereafter referred to as Tsunami Run-up Response Function-based INVersion or TRRF-INV model. This study provides the first tsunami inversion model capable of giving probabilistic estimates of tsunami source information (moment magnitude, epicenter location, fault length, fault width, and average slip) from tsunami run-up records. Moreover, to our best knowledge, our work is the first attempt to provide probabilistic estimates of tsunami run-up distribution derived only from a small number of tsunami run-up records. We chose the northern Chile coastal region as a study area and investigated the performance of the TRRF-INV model based on synthetic tsunami run-up records, and then we applied the TRRF-INV model to real tsunami run-up records of the M_W 8.2 2014 Iquique, Chile, earthquake.

2. Study Area

The northern Chile coastal area is an active subduction zone where the Nazca plate is being subducted under the continental South American plate at high rates (about 63 mm/year, Chlieh et al., 2011) (Figure 1). The city of Iquique, one of the important commercial and industrial urban centers in the northern Chile coastal region, is exposed to significant tsunami risk considering its inhabitants (about 184,000) and critical coastal infrastructures (González et al., 2020). Historically, large earthquakes (M_W >8.5) occurred in 1868 and 1877 near the convergent tectonic plate interface, and the tsunamis damaged the cities in northern
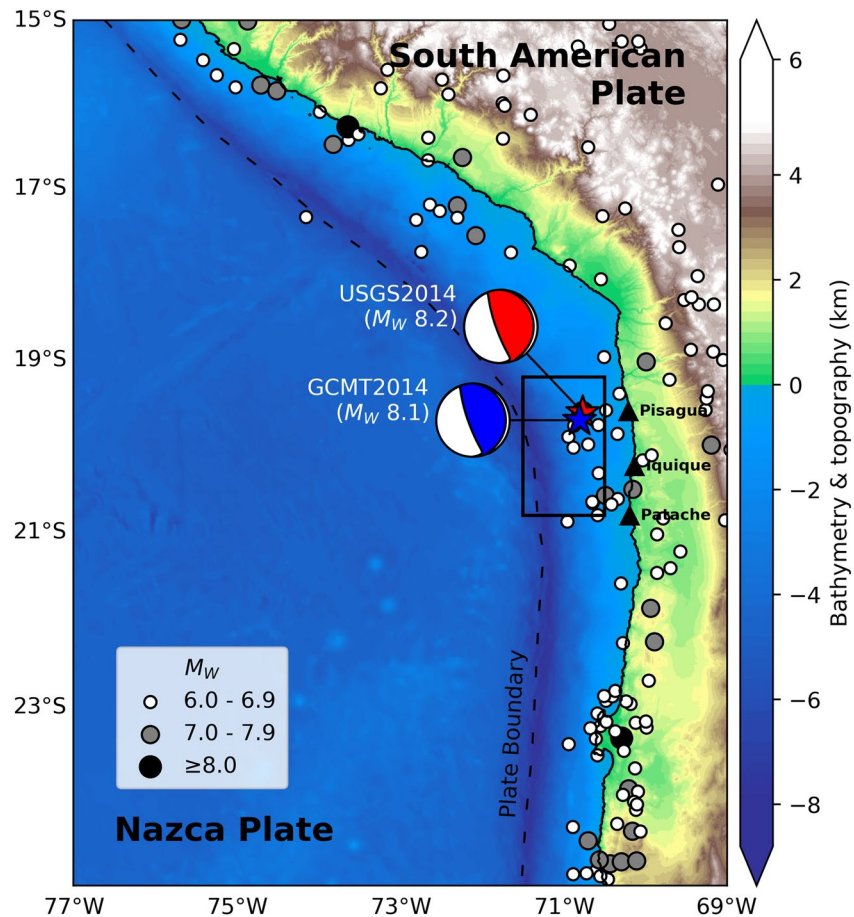
Figure 1. Map of the northern Chile coastal region. The circles represent the historical earthquake records with magnitude larger than 6 (U.S. Geological Survey National Earthquake Information Center). The black dashed line represents the plate boundary between the Nazca and South American plates. Focal mechanisms (beachballs) and epicenters (stars) of the 2014 Iquique earthquake given by the USGS and the gCMT (Ekström et al., 2012) are plotted in red and blue colors, respectively. The locations of Patache, Iquique, and Pisagua are shown in black triangles. The black rectangle represents the possible tsunami source area used in this study.

Chile coastal region (González et al., 2020; Kulikov et al., 2005). On April 1, 2014, at 23:46:50 UTC, an M_W 8.2 earthquake occurred off the coast of Pisagua in northern Chile in an area known as a seismic gap (a portion of an active fault known to cause a major earthquake but not occurring for a long time) (Hayes et al., 2014). This earthquake was detected in the form of a seismic waveform, strong motion, and GPS data, and the resulting tsunami was visually detected in several DART buoys and tide gauges (e.g., An et al., 2014; Gusman et al., 2015; Lay et al., 2014; Schurr et al., 2014; Sepúlveda et al., 2017). Moreover, high-quality tsunami run-up records also exist (Catalán et al., 2015). Even though the 2014 Iquique earthquake relieved some amount of the accumulated deviatoric stress, several studies pointed out that the northern Chile coastal region still can generate a large earthquake with an associated tsunami (Cesca et al., 2016; Ruiz et al., 2015).

3. Method

The TRRF-INV model infers a tsunami source and tsunami run-up distribution from run-up records in four steps as follows (Figure 2):

- Step 1: Set three angles (strike, dip, and rake) and earthquake depth
- Step 2: Determine the order in which to estimate the fault parameters (epicenter latitude, epicenter longitude, fault length, fault width, and average slip)
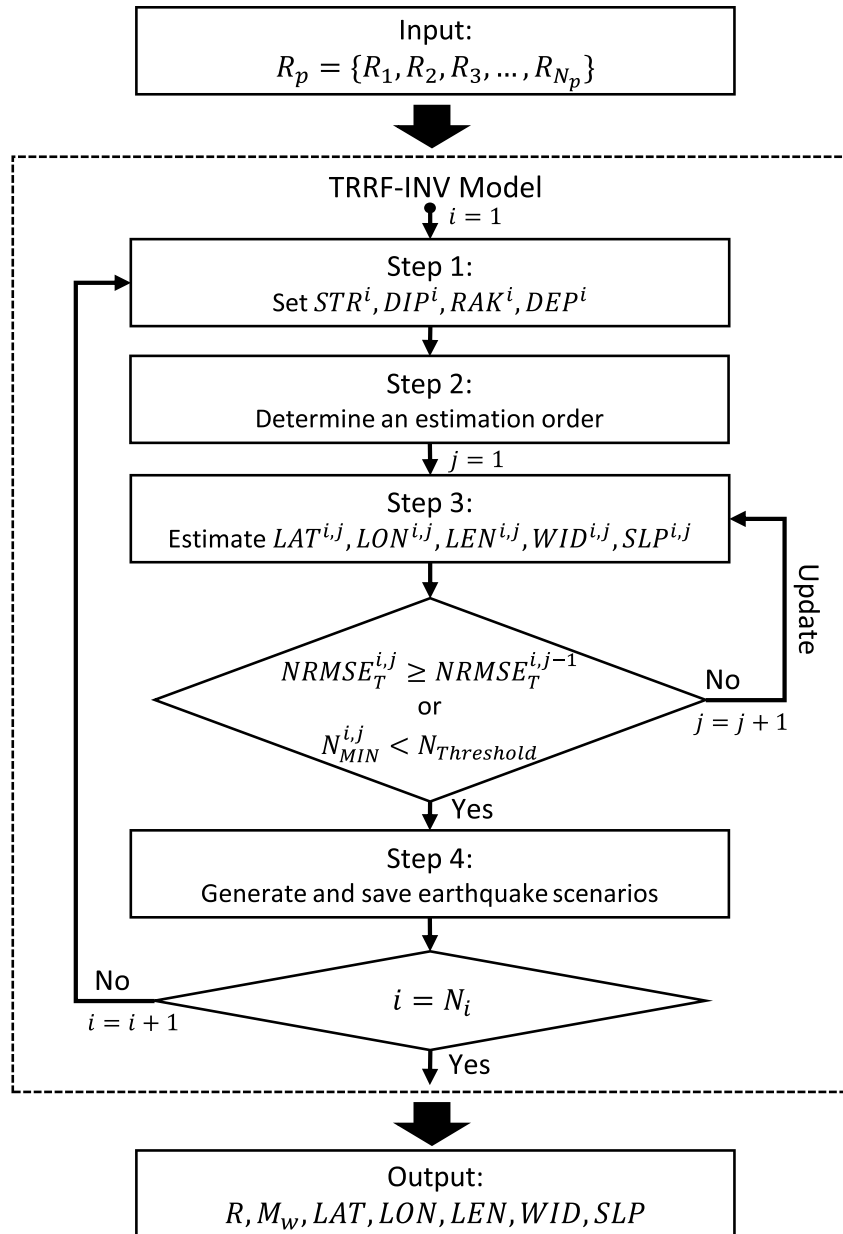
Figure 2. Computational flow of TRRF-INV model. The inputs are tsunami run-up records (R_p) where N_p represents the number of run-up records. The outputs are the probabilistic estimates of moment magnitude (M_W), epicenter latitude (LAT), epicenter longitude (LON), fault length (LEN), fault width (WID), average slip (SLP), and tsunami run-up distribution (R). N_i is the number of combinations of three angles and earthquake depth. j is the iteration number. $NRMSE_T$ is a total error. N_{MIN} is the minimum number of earthquake scenarios. Note that the epicenter is the centroid of the fault.

- Step 3: Repeat estimating fault parameters until one of two thresholds (see Section 3.3) is satisfied
- Step 4: Generate earthquake scenarios based on the estimated fault parameters and save possible scenarios

The TRRF-INV model repeats these four steps and accumulates possible earthquake scenarios until all fault geometry combinations defined in step 1 are considered. And lastly, the probabilistic tsunami source and tsunami run-up distribution are estimated based on the accumulated scenarios.

Table 1
Fault Parameters Used for TRRF Training, Calibration, and Validation

	Training			Calibration and validation	
Fault parameter	Low	Central	High	Min	Max
LON (°W)	70.5	71.0	71.5	70.5	71.5
DIP (°)	10	20	30	10	30
LEN (km)	90	135	180	90	180
WID (km)	40	75	90	40	90
SLP (m)	2	4	6	2	6
DEP (km)	10	25	40	10	40
LAT (°S)		20		19.2	20.8
STR (°)		360		340	360
RAK (°)		90		70	110

To run the TRRF-INV model, a pretrained TRRF model for the study area is required. In this study, we trained the TRRF model based on physics-based numerical simulations of 729 tsunamigenic-earthquake scenarios (Table 1) following Lee et al. (2020). A description of how the range of each fault parameter is determined can be found in Appendix A. We used the numerical model Basilisk, an efficient hydrodynamic numerical model that employs an Adaptive Mesh Refinement (AMR) technique and a parallel computing technique (Popinet, 2015). We set the *x*-axis parallel to North and *y*-axis parallel to West. We systemically simulated additional 175 scenarios to calibrate the TRRF model. Then, to validate the TRRF model, we simulated 20 random scenarios (hereafter called base scenarios), which were never used to train or calibrate the TRRF model (Table S1). The error of the TRRF model was represented by a normalized root-mean-square error (*NRMSE*); the *RMSE* normalized by the maximum run-up:

$$NRMSE = \frac{\sqrt{\frac{1}{N_p}\sum_{x=1}^{N_p}\left[R_T(x) - R_p(x)\right]^2}}{max\left[R_p(x)\right]} \times 100(\%) \tag{1}$$

where $R_T(x)$ is the tsunami run-up predicted by the TRRF model, $R_p(x)$ is the true tsunami run-up (Basilisk predictions or observational data), and N_p is the number of alongshore locations considered. More details on the TRRF model training, calibration, and validation can be found in Appendix A.

The TRRF-INV model also requires a predefined range of fault parameters. In this study, we set the fault-parameter range as shown in Table 2, which is within the range used for TRRF model validation. The rest of the section will describe the details of the TRRF-INV model.

3.1. Step 1: Set Three Angles and Earthquake Depth

Step 1 is to set the fault geometry (strike *STR*, dip *DIP*, rake *RAK*, and top-edge fault depth *DEP*). Most of the existing tsunami inversion models fixed the fault geometry to one setting because of the computational burden of tsunami forward simulations. However, if the uncertainty of the fault geometry is ignored, the tsunami source may not be reliably estimated (Ragon et al., 2018). Thus, the TRRF-INV model is designed to consider the uncertainty of the fault geometry by considering several combinations of fault geometry.

In this study, we considered 27 combinations ($N_i = 27$) where three-level values of *STR*, *DIP*, *DEP* and one *RAK* are considered (Table 2). The range of *STR*, *DIP*, and *DEP* was determined based on the Slab model values in the study area (Hayes et al., 2018). Since the *NRMSE* changes only up to 1% with rake angle over the range from 70°−110°, we assumed a pure reverse-slip mechanism (*RAK* = 90°). Note that the range of *STR*, *DIP*, and *RAK* used in this study is similar to the fault geometry used in the integrated tsunami forecast and warning system in Chile (Catalan et al., 2020).

Table 2
The Range of Fault Parameters With Interval Used in the TRRF-INV Model

Fault parameter	Min	Max	Interval
LON (°W)	70.5	71.5	0.1
LAT (°S)	19.2	20.8	0.1
LEN (km)	90	180	5
WID (km)	40	90	5
SLP (m)	2	6	0.5
DEP (km)	20	30	5
STR (°)	340	360	10
DIP (°)	10	30	10
RAK (°)	90	90	0

3.2. Step 2: Determine an Estimation Order

Even though the TRRF model is rapid (computational time: <1 s/scenario), it is still computationally intensive to simulate all possible scenarios listed in Table 2 (>9 million scenarios). To minimize the number of TRRF simulations, the TRRF-INV model determines the order in which to estimate the fault parameters (epicenter latitude *LAT*, epicenter longitude *LON*, fault length *LEN*, fault width *WID*, and average slip *SLP*) as follows.

First, the TRRF-INV model generates scenarios for each of the five fault parameters (hereafter a reference fault parameter) as follows. The reference fault parameter varies for all values in Table 2. The other four fault parameters vary for three-level values (minimum, maximum, and average of values listed in Table 2). The three angles and the earthquake depth are fixed to the values set in step 1. Note that the interval of five fault parameters in Table 2 was set to the value where the *NRMSE* change within the interval is negligible (<0.5% point). Second, tsunami run-ups are estimated based on the TRRF model for each scenario, and then the *NRMSE* between the TRRF estimates and the run-up records is calculated. Third, the scenarios where the reference fault parameter value is the same are grouped, and the mean error ($\overline{NRMSE}$) is calculated for each group. Fourth, the maximum difference of $\overline{NRMSE}$ among groups ($\Delta\overline{NRMSE}$) is calculated. And lastly, once the $\Delta\overline{NRMSE}$ is calculated for all fault parameters (*LAT*, *LON*, *LEN*, *WID*, *SLP*), the estimation order is defined as an order from the most sensitive fault parameter (which shows the largest $\Delta\overline{NRMSE}$) to the least sensitive fault parameter (which shows the smallest $\Delta\overline{NRMSE}$) (see example result in Text S1 and Figure S1).

3.3. Step 3: Estimate Fault Parameters

Following the estimation order, the fault parameters are estimated until one of two stop conditions is satisfied: (1) when the error does not decrease compared to the previous iteration, (2) when the number of generated scenarios is less than the threshold. From now on, the fault parameter of the ith combination (three angles and depth) of the jth iteration of kth estimation order will be represented as $FP_k^{i,j}$.

To estimate the first-order fault parameter ($FP_1^{i,j}$), the TRRF-INV model generates scenarios for each value of the FP_1 in Table 2 as follows. If it is the first iteration ($j = 1$), the TRRF-INV model generates scenarios considering all combinations of three-level values of FP_2, FP_3, FP_4, and FP_5 used in step 2. Otherwise, the TRRF-INV model generates scenarios considering all combinations of the ($j - 1$)th estimates of the other four fault parameters ($FP_2^{i,j-1}, FP_3^{i,j-1}, FP_4^{i,j-1}, FP_5^{i,j-1}$). The three angles and the earthquake depth are fixed to the values set in step 1. Second, tsunami run-ups are estimated based on the TRRF model for each scenario, and then the *NRMSE* between the TRRF estimates and the run-up records is calculated. Third, the scenarios where the FP_1 value is the same are grouped, and the base group is defined as a group that shows the smallest mean error ($min(\overline{NRMSE}_{FP_1}^{i,j})$). Fourth, the model conducts the Welch's t-test between the base group and the other groups. Based on the t-test result, the estimates of the $FP_1^{i,j}$ are defined as the FP_1 values corresponding to the base group and the other groups that show no statistically significant $\overline{NRMSE}$ difference compared to that of the base group (p-value >0.05).

The other four fault parameters are estimated in the same way, following the estimation order. The only difference is that, when generating the scenarios to estimate the present-order fault parameter, the jth estimates of the preceding-order fault parameters are used instead of the ($j - 1$)th estimates. For example, when estimating the fault parameter of the ith combination (three angles and depth) of the jth iteration of the third-order ($FP_3^{i,j}$), the jth estimates of the first- and second-order fault parameters ($FP_1^{i,j}, FP_2^{i,j}$) are used to generate the scenarios, instead of the ($j - 1$)th estimates ($FP_1^{i,j-1}, FP_2^{i,j-1}$).

Once all fault parameters ($FP_k^{i,j}$) are estimated, the total error ($NRMSE_T^{i,j}$) and the minimum number of generated earthquake scenarios ($N_{MIN}^{i,j}$) are calculated:

$$NRMSE_T^{i,j} = \sqrt{\sum_{k=1}^{5}(min(\overline{NRMSE}_{FP_k}^{i,j}))^2} \qquad (2)$$

$$N_{MIN}^{i,j} = min(N_{FP_k}^{i,j}) \quad where\ k = 1, 2, \ldots, 5 \qquad (3)$$

where $N_{FP_k}^{i,j}$ is the number of earthquake scenarios in the base group to estimate the $FP_k^{i,j}$. Then the TRRF-INV model decides whether to stop the iteration based on the two stop conditions:

$$NRMSE_T^{i,j} \geq NRMSE_T^{i,j-1} \tag{4}$$

$$N_{MIN}^{i,j} < N_{Threshold} \tag{5}$$

The first stop condition (Equation 4) is when the total error is not reduced compared to the previous iteration. Note that the first stop condition is only checked after the second iteration ($j \geq 2$). The second stop condition (Equation 5) is when the minimum number of generated earthquake scenarios is less than the threshold ($N_{Threshold}$). The larger the threshold, the less precise the model is, and the smaller the threshold, the more likely the error distribution is not to satisfy normality. In this study, we set the threshold ($N_{Threshold}$) to 10, balancing the model precision and normality of the error distribution. If one of the stop conditions is satisfied at the jth iteration, the model stops estimating the fault parameters, and the fault parameter estimates of the ($j - 1$)th iteration are saved. Otherwise, the TRRF-INV model will repeat the procedure mentioned above (see example result in Text S2 and Figure S2).

3.4. Step 4: Generate and Save Earthquake Scenarios

The last step is to generate the earthquake scenarios based on the estimated fault parameters and save the possible scenarios where the *NRMSE* is smaller than the threshold. To be specific, the TRRF-INV model calculates the moment magnitude using the following equations (Aki, 1966; Hanks & Kanamori, 1979):

$$M_W^i = \frac{2}{3}\Big[\log\big(M_o^i\big) - 9.05\Big] \tag{6}$$

$$M_o^i = \mu(LEN^i \times WID^i \times SLP^i) \tag{7}$$

where M_o is a seismic moment (Nm), μ is the rigidity modulus of the Earth's crust (Nm^{-2}), and the units of fault length (*LEN*), fault width (*WID*), and average slip (*SLP*) are in meters. In this study, we assumed that the rigidity modulus μ is 3.5×10^{10} Nm^{-2} in northern Chile coastal region following Shrivastava et al. (2019). Second, the TRRF-INV model generates scenarios considering all combinations of the estimated epicenter (LAT^i, LON^i) and the three fault parameters (*LEN*, *WID*, *SLP*) within the range of moment magnitude (M_W^i). The three angles and the earthquake depth are fixed to the values set in step 1. Third, tsunami run-ups are estimated based on the TRRF model for each scenario, and then the *NRMSE* between the TRRF estimates and the run-up records is calculated. Finally, the TRRF-INV model saves the earthquake scenarios where the corresponding *NRMSE* values are smaller than the threshold ($NRMSE_{Threshold}^i$) defined as follows:

$$NRMSE_{Threshold}^i = min\big(\mathbf{NRMSE}^i\big) + \alpha\Big[max\big(\mathbf{NRMSE}^i\big) - min\big(\mathbf{NRMSE}^i\big)\Big] \tag{8}$$

where $\mathbf{NRMSE}^i$ is a list of the *NRMSE* values of the generated scenarios, and α is a constant that determines the threshold. In this study, after testing various α values, we set the α to 0.2 to balance the efficiency and the accuracy of the TRRF-INV model (Text S3 and Figure S3).

The TRRF-INV model repeats the process from step 1 to step 4 until all combinations of three angles and earthquake depth are considered ($i = N_i$). Once all combinations are considered, the TRRF-INV model estimates the probabilistic tsunami source and tsunami run-up distribution based on the accumulated earthquake scenarios.

4. Results

4.1. Performance on Synthetic Scenarios

To validate the TRRF-INV model, we generated 200 synthetic scenarios as follows. For each of the 20 base scenarios (Table S1), we made 10 scenarios by randomly selecting a few run-ups from the tsunami run-up distribution of Basilisk simulation. In this test, we fixed the number of run-up records ($N_p = 20$) to make the number of run-ups similar to the 2014 Iquique tsunami run-up record. Note that only these 20 run-up data
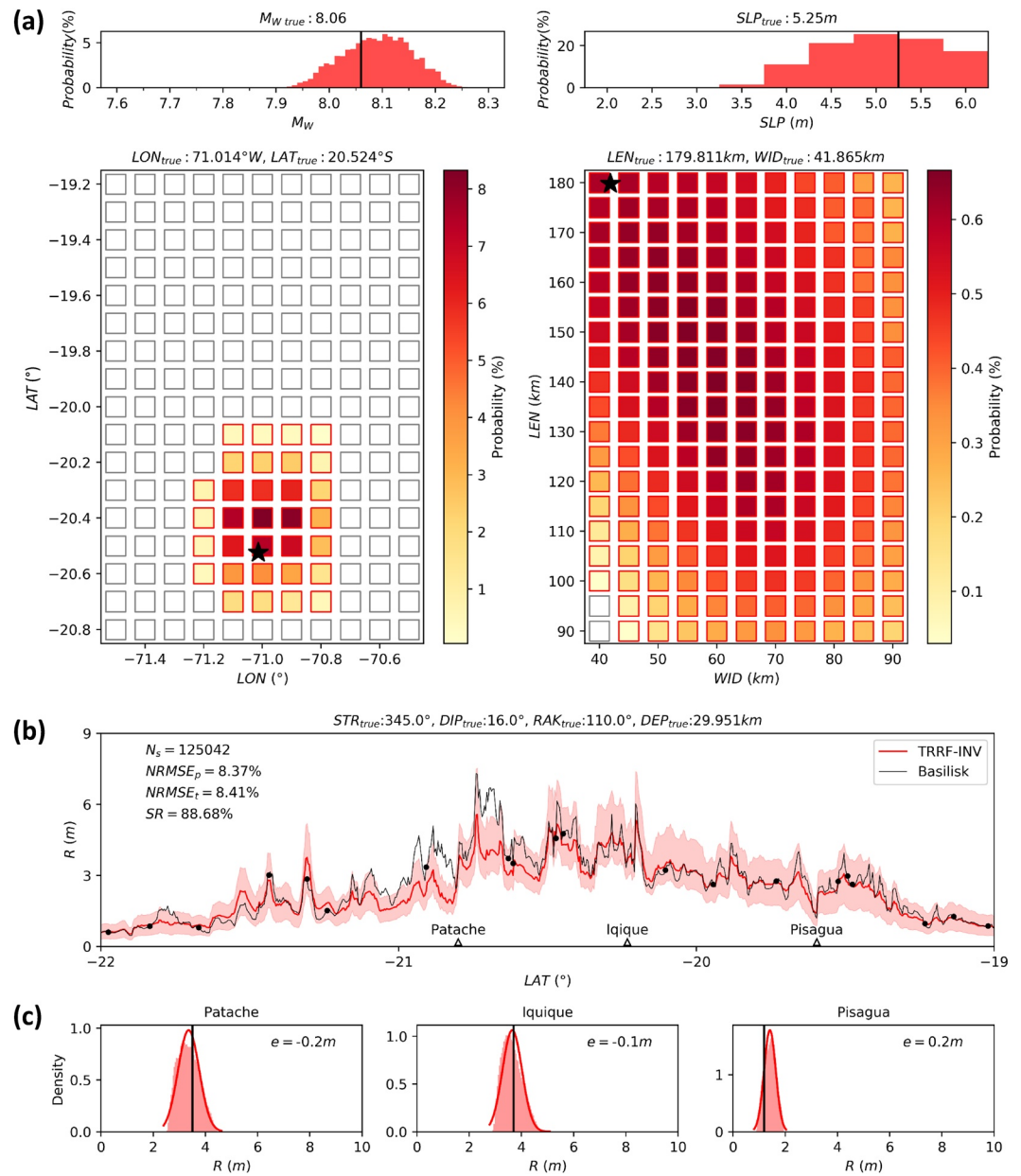
Figure 3. The TRRF-INV model outputs for the synthetic scenario. (a) Probabilistic estimates of tsunami source where the black lines and stars represent the true values (uniform slip assumed). (b) Probabilistic tsunami run-up distribution. The light red area represents the full range of run-up, and the red line represents the median. The black line is true tsunami run-up distribution. The black circles are the input of the TRRF-INV model. (c) The probability density function (red curve) compared to the true run-up (black line) at three locations.

were provided to the TRRF-INV model as an input while the true values (the earthquake fault parameters and the tsunami run-up distribution) were intentionally concealed during the TRRF-INV model run. Here, we will first present the detailed result based on one of the synthetic scenarios (Figure 3) and then highlight the overall performance of the TRRF-INV model (Figure 4).

Figure 3 shows the results of the scenario with the smallest error for moment magnitude but the largest error for the tsunami run-up distribution among the 10 random scenarios for Case 1 in Table S1. Overall, the probabilistic estimates of tsunami source agree well with the true values for this synthetic scenario (Figure 3a). We defined the error (*e*) as the estimated value (that showed the highest probability) minus
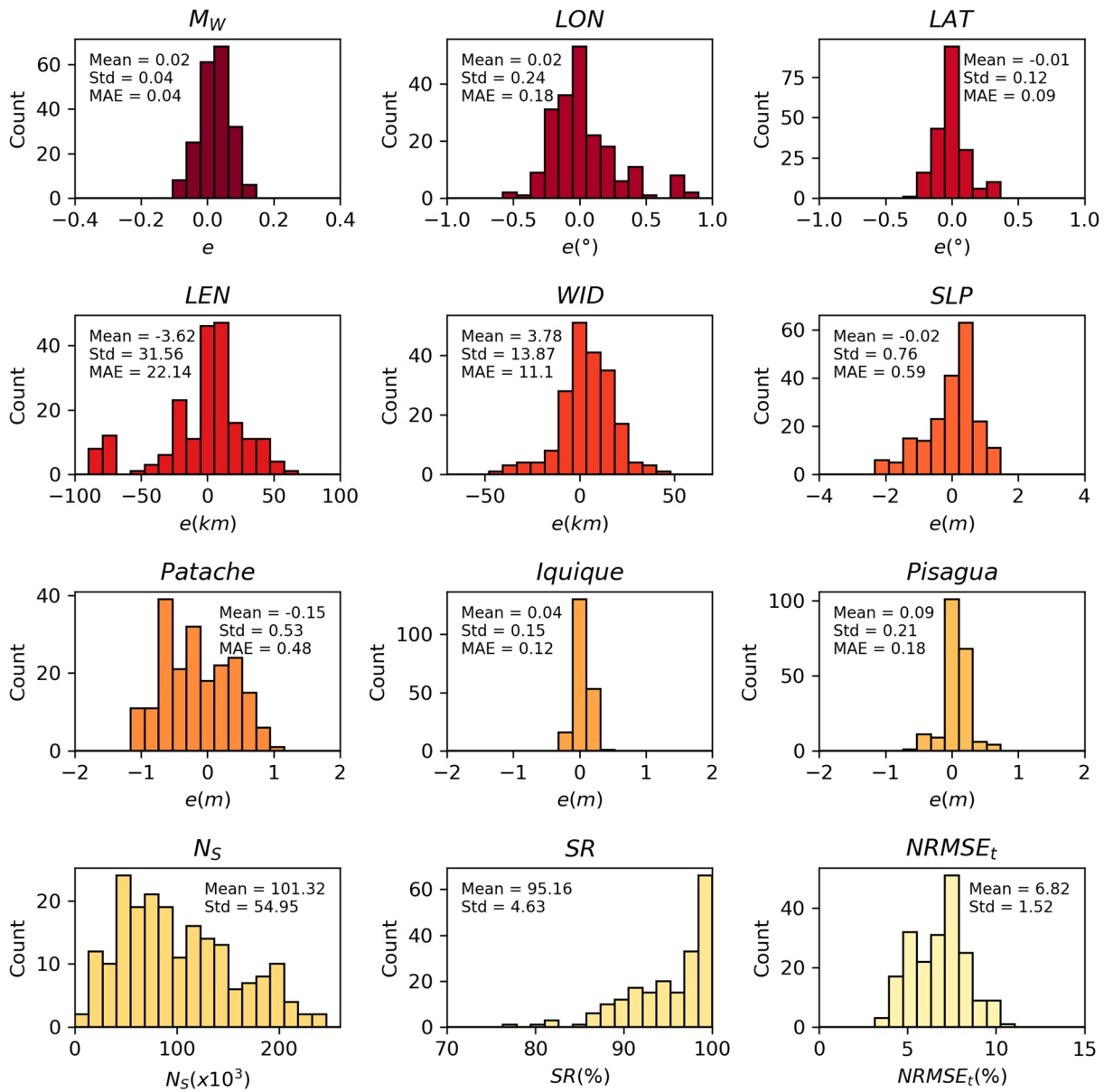
Figure 4. Performance of the TRRF-INV model based on 200 synthetic scenarios. The top three rows show the error (e) distribution of moment magnitude (M_W), epicenter longitude (LON), epicenter latitude (LAT), fault length (LEN), fault width (WID), average slip (SLP), and the run-ups at three key locations (Patache, Iquique, and Pisagua) where the e is defined as the estimated value minus the true value, and the MAE represents the mean absolute error. The bottom row shows the histograms of the number of filtered scenarios (N_S), success rate (SR), and the normalized root-mean-squared error ($NRMSE_t$). The mean and the standard deviation (Std) are denoted within each panel.

the true value. The TRRF-INV model slightly overestimated the M_W ($e = 0.04$), LON ($e = 0.014°$), LAT ($e = 0.124°$), and WID ($e = 19$ km), while the model slightly underestimated the SLP ($e = −0.25$ m). Even though the LEN shows a relatively large error ($e = −39$ km), the true value falls within the high probability region (>0.6%). In Figure 3b, we plot the probabilistic estimate of the tsunami run-up distribution. The result shows that the probabilistic estimate of the TRRF-INV model agrees well with the true tsunami run-up distribution, except near the underestimated Patache area. The $NRMSE$ between the true value and median of estimates was 8.37% when we only compared the 20 input locations ($NRMSE_p$) and 8.41% when we compared the entire locations ($NRMSE_t$). We defined a success ratio (SR) as a ratio of the number of locations where the true run-up value falls within the range of run-up estimates (light red area in the upper
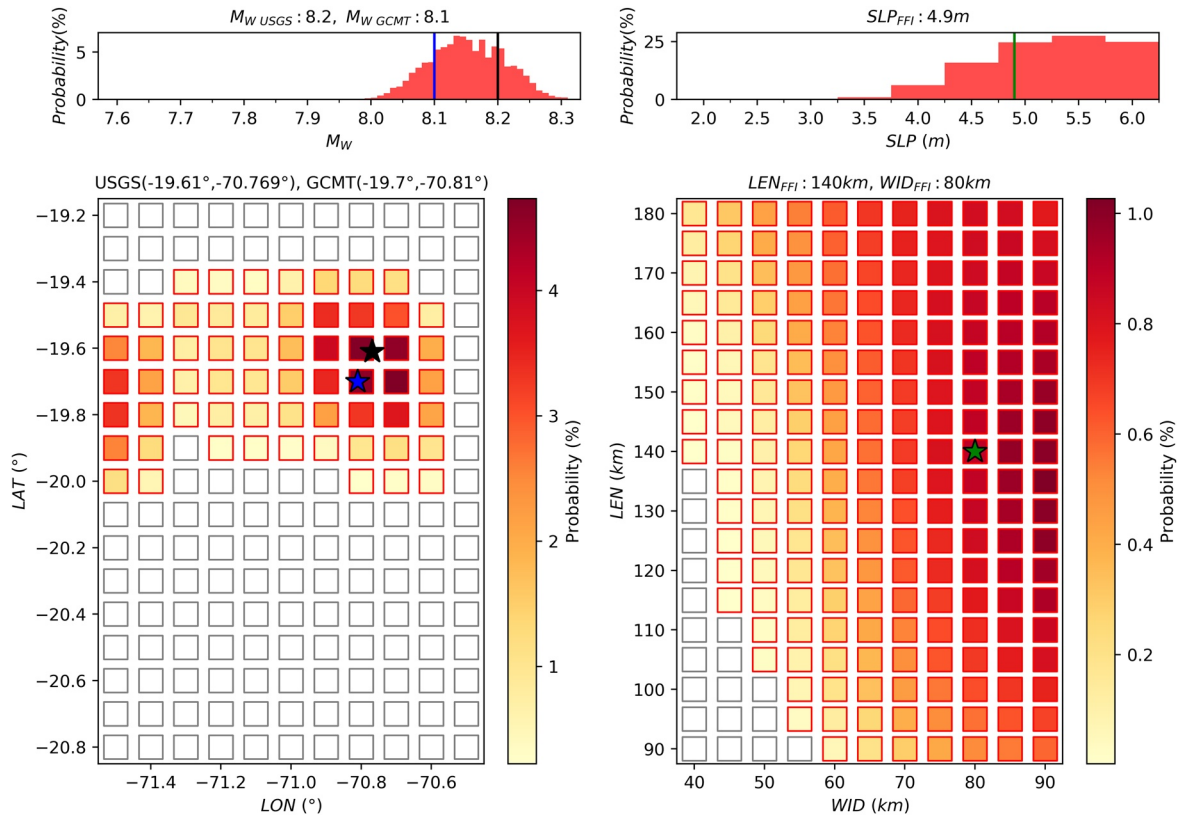
Figure 5. Probabilistic estimates of tsunami source based on the 2014 Iquique tsunami run-up records. The black line and star represent the United States Geological Survey (USGS) report result. The blue line and star represent the global Centroid Moment Tensor (GCMT) solution. The green line and star represent the An et al. (2014)'s finite fault inversion (FFI) model result.

panel of Figure 3b). Moreover, the error (e) of run-up at three key locations (Patache, Iquique, and Pisagua, see Figure 1) was calculated by subtracting the true value from the median of the fitted distribution. In the case shown in Figure 3, the TRRF-INV model yields the SR of 88.68% and small errors at three key locations ($|e| \leq 0.2$ m).

Figure 4 summarizes the result of all 200 synthetic scenarios where MAE represents the mean absolute error.

$$MAE = \left(\frac{1}{n}\right)\sum_{i=1}^{n}|e_i| \tag{9}$$

where e_i is the error of the ith scenario and n is the total number of scenarios. Overall, the TRRF-INV model provides a reasonable first-order estimates of tsunami source, especially for the moment magnitude M_W ($MAE = 0.04$), and the epicenter latitude LAT ($MAE = 0.09°$). Moreover, the TRRF-INV model estimates the tsunami run-up distribution quite well only with the 20 run-up data (mean $SR = 95.16\%$), especially in Iquique ($MAE = 0.12$ m) and in Pisagua ($MAE = 0.18$ m). The mean $NRMSE_t$ is about 6.82%, which is similar to the error of the TRRF model itself.

4.2. Performance Using the 2014 Iquique Tsunami Run-up Records

To evaluate the performance of the TRRF-INV model on a real tsunami event, we applied the TRRF-INV model to infer the tsunami source and tsunami run-up distribution from the 2014 Iquique tsunami run-up records (Catalán et al., 2015) and then compared our results with the United States Geological Survey (USGS) report, the global Centroid Moment Tensor (gCMT) solution, and the other tsunami inversion mod-
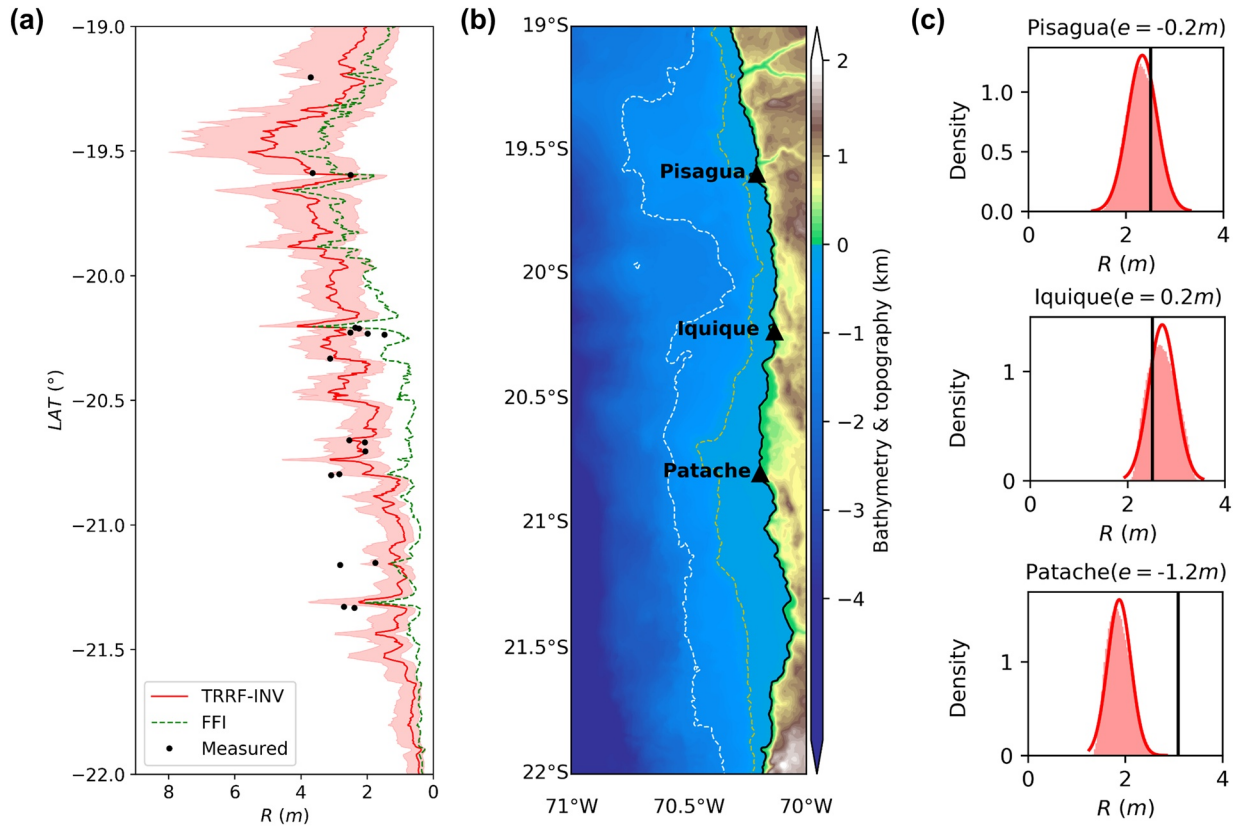
Figure 6. (a) A probabilistic tsunami run-up distribution based on the 2014 Iquique tsunami run-up records. The light red area represents the full range of estimated run-up, and the red line represents the median. The green dashed line is a tsunami run-up distribution based on the An et al. (2014)'s finite fault inversion (FFI) source, and the black circles are the 2014 Iquique tsunami run-up records. (b) Bathymetry map of the study area. Yellow and white dashed lines represent the −200 and −1000 m isobaths. (c) The probability density function of the TRRF-INV model estimates (red curve) compared to the measured run-up (black line) at three key locations.

el result (An et al., 2014). To match the resolution of run-up records with the grid interval of the TRRF-INV model (0.004°), we used the mean value if there were more than one run-up record within a grid.

Figure 5 shows the first output of the TRRF-INV model based on the 2014 Iquique tsunami run-up records. The results show that the estimated M_W (= 8.13) falls within the range between the M_W of gCMT and that of USGS. The estimated epicenter (−19.7°, −70.7°) strongly agrees with the epicenter of USGS and that of gCMT. The relatively large probability, though not the largest, was shown near the plate boundary (−19.8°, −71.5°). Since there is no true value for the fault geometry (LEN, WID, SLP), we compared the TRRF-INV model result with the An et al. (2014)'s finite fault slip distribution. The estimated slip ($SLP = 5.5$ m) is slightly larger than the average slip of An et al. (2014). The estimated fault length ($LEN = 135$ km) and fault width ($WID = 90$ km) resembles the fault size of An et al. (2014). Note that we defined the average slip and the fault size of the An et al. (2014)'s slip distribution based on the finite faults where the slip is larger than 3 m.

Figure 6 shows the second output of the TRRF-INV model based on the 2014 Iquique tsunami run-up records. The results show that the tsunami run-up distribution based on the TRRF-INV model is reasonably matched with the run-up records. The estimated run-ups at Iquique and Pisagua agree with the observations very well ($|e| = 0.2$ m), while the TRRF-INV model underestimates the observed run-up of 1.2 m at Patache (see Figure 6c). Note that we used the nearest run-up records to compare the run-ups at three key locations. To compare the performance of the TRRF-INV model and other tsunami inversion models in estimating the tsunami run-up distribution, we simulated the 2014 Iquique tsunami based on the An et al. (2014)'s tsunami source using the same Basilisk simulation condition used to develop the TRRF model

in this study. The tsunami run-up distribution estimated by the An et al. (2014)'s tsunami source shows a larger error ($RMSE_p$ = 1.37 m) than the TRRF-INV model result ($RMSE_p$ = 0.87 m), underestimating the tsunami run-ups, especially in the area between the Patache and Iquique.

5. Discussion

Even though there was a couple of synthetic scenarios that showed a poor agreement in a tsunami source and/or run-ups, it is worth noting that the TRRF-INV model provides reasonable first-order estimates in most of the cases, given that the TRRF-INV model only used the 20 run-up data.

In the 200 synthetic-scenario test (Figure 4), the mean absolute error (*MAE*) of the epicenter latitude (*LAT*) was twice smaller than that of the epicenter longitude (*LON*). This may be attributed to the orientation of the coastline and the earthquake fault used in this study. We assumed that the coastline was parallel to the north-south direction, and the strike direction was parallel or inclined up to 20° to the coastline. In this condition, the change of the tsunami run-up distribution is more sensitive to the epicenter latitude (*LAT*), and thus the TRRF-INV model can distinguish a relatively small change of the epicenter latitude (*LAT*). Similarly, the fact that the change of the tsunami run-up distribution was more sensitive to the fault width (*WID*) than the fault length (*LEN*) can explain the mean absolute error (*MAE*) of the fault width (*WID*) that was twice smaller than that of the fault length (*LEN*).

The TRRF-INV model shows a relatively large run-up error in Patache even though the average run-up of 20 base scenarios (Table S1) in Patache was similar to that in Iquique and Pisagua (Figure 4). Similar pattern was also found in the case study of the 2014 Iquique tsunami (Figure 6). We interpret this large error at Patache as a result of the tsunami-source direction that was mostly oriented toward the Iquique-Pisagua area (Table S1). In this condition, tsunami waves arrived at Patache would have been relatively more affected by the secondary factors related to the local bathymetry effects (Catalán et al., 2015; González et al., 2020), which is not directly considered in the TRRF model, than the tsunami waves at Iquique and Pisagua.

In Figure 5, the TRRF-INV model slightly overestimated the slip and the fault size compared to the average slip and the fault size of the An et al. (2014)'s slip distribution. This may be attributed to the bathymetry/topography grid resolution, and the uniform slip distribution assumption in TRRF-INV modeling. To be specific, we used the 15 arc-second resolution grid (GEBCO Compilation Group, 2019) to model the tsunami inundation process. However, several studies showed that numerical simulations based on coarser grid resolution (>50 m) might underestimate the run-up (e.g., Muhammad & Goda, 2018). Similar behavior was observed for the 2014 Iquique tsunami simulation in Catalán et al. (2015). Catalán et al. (2015)'s run-up predictions fit well with the 2014 Iquique tsunami observations for the area where the higher resolution grid (1 arc-second) was used, and the run-up predictions were underestimated for the area where the lower resolution grids (120, 30, and 6 arc-second) were used. Second, it is well known that uniform slip distribution may underestimate the run-up (Becerra et al., 2020; Carvajal & Gubler, 2016; Geist & Dmowska, 1999; Melgar et al., 2019). On that ground, the TRRF-INV model may overestimate the slip and the fault size when fitting the tsunami run-up observations. Similarly, the underestimation of run-up in the numerical simulation based on An et al. (2014)'s slip distribution in Figure 6 may be attributed to the bathymetry/topography grid resolution.

In the 2014 Iquique tsunami case, the largest run-up was predicted near the epicenter latitude, with run-up becoming smaller with increased distance from the epicenter latitude (see red line in Figure 6a). A relatively small run-up was predicted at Pisagua compared to the run-up in the nearby region. This may be related to the coastal morphology at Pisagua, which has a narrow platform less than 150 m wide between the coastline and the coastal cliff, while the surrounding area is dominated by tall, steep coastal cliffs (Catalán et al., 2015). Overall, a relatively larger run-up is associated with the presence of large-scale bays (see Figure 6b). This may be due to the shelf resonant at large-scale bays, as discussed in Catalán et al. (2015). However, it should be noted that since this study only simulated 2 h of tsunami elapsed time, the results may not capture some of the long period oscillations and the resulting late arrival peak run-up that could be caused by the shelf resonant and edge waves.
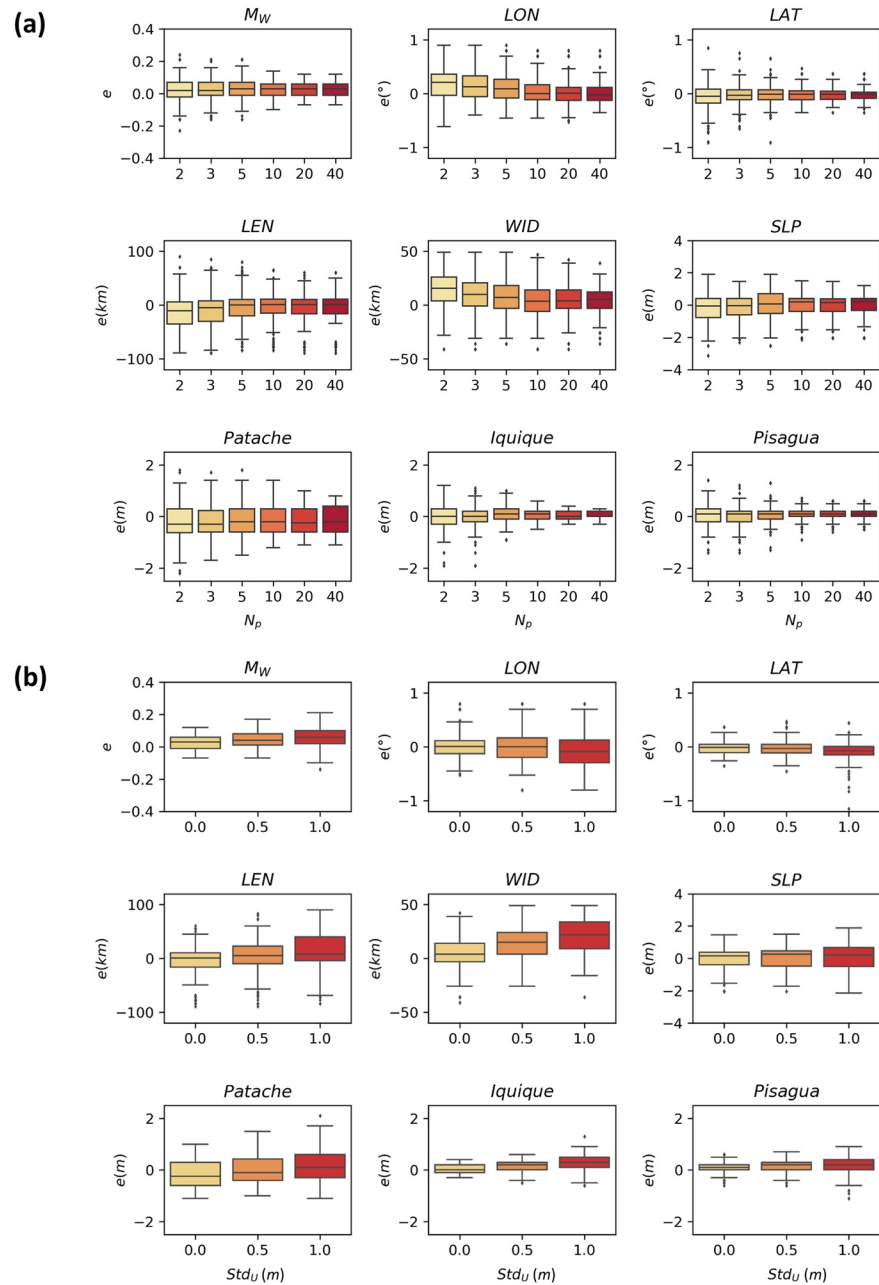
Figure 7. Performance of the TRRF-INV model depending on (a) the number of run-up records (N_p) and (b) the uncertainty of run-up records. The error (e) is defined as the estimated value minus the true value. The Std_U represents the standard deviation of uncertainty in meters. Each box-whisker plot consists of 200 random scenarios. The box symbol shows the interquartile range (box boundary) and median (horizontal line). The lower (upper) whisker is defined as 1.5 times the interquartile range below (above) the first (third) quartile. The data beyond the whiskers are plotted as an outlier (diamond).

We conducted two additional tests to analyze the sensitivity of the TRRF-INV model depending on the number and the uncertainty of run-up records (Figure 7, Figures S4–S11). First, we investigated the performance of the TRRF-INV model depending on the number of run-up records (N_p = 2, 3, 5, 10, 20, 40) (Figure 7a). For each number (N_p), a total of 200 scenarios were considered by generating 10 random scenarios for each of the 20 base scenarios (Table S1). The results showed that the error (e) decreased as the number of run-up records (N_p) increased in general. Note that the performance is similar after N_p = 20 because of the error the TRRF model itself has. Second, we investigated the performance of the TRRF-INV model as

the uncertainty of run-up records increased (Figure 7b). The number of run-up records ($N_p = 20$) was fixed, and the uncertainty of run-up values was generated randomly from a normal distribution with a standard deviation ($Std_U = 0$, 0.5, 1.0 m) and zero mean. For the input run-ups that showed negative values after considering the uncertainty, we replaced them with zeros to prevent unrealistic negative run-up values. The results showed that the error (e) increased as the uncertainty of run-up increased in general. The TRRF-INV model tends to overestimate the moment magnitude (M_W), fault length (LEN), fault width (WID), average slip (SLP), and run-ups at three key locations as the uncertainty increases. This is because the number of input run-ups replaced by zero is likely to increase as the uncertainty increases. These two tests suggest that the optimum conditions for achieving the convergent performance of the TRRF-INV model in northern Chile are approximately 20 observed run-up records with less than 0.5 m of uncertainty.

It is important to note that the performance of the TRRF-INV model depends on not only the run-up records but also several other factors such as uncertainty in fault parameter range and earthquake slip complexity. To be specific, we assumed that the fault parameter range in Table 2 is large enough to represent the uncertainty of fault parameter. However, depending on the target earthquake event (e.g., ancient earthquake events), the uncertainty in fault parameter range may be larger than the fault parameter range considered here and shown in Table 2. Thus, future studies should evaluate how the accuracy and efficiency of the TRRF-INV model vary as the fault parameter range changes. Second, we only tested the TRRF-INV model for up to about M_W 8.3 earthquake, assuming a uniform slip distribution. And, the 2014 Iquique earthquake rupture can be considered as a compact and centered slip distribution compared to other large earthquakes (Chen et al., 2016). Thus, it is necessary to investigate further the performance of the TRRF-INV model for larger magnitude earthquakes with more complex slip distributions.

6. Conclusions

The capability to understand a tsunami source and its impact is crucial in robust tsunami hazard assessment. To date, several tsunami inversion models have been developed, relying on several types of measured data such as seismic waveform, strong motion, GPS, InSAR, DART, and tide gauge data. Compared to these data, a tsunami run-up record has not been used widely to infer a tsunami source and tsunami run-up distribution because of the computational burden of tsunami forward simulations. In this study, we propose a new tsunami inversion model, called TRRF-INV model, which can infer a probabilistic near-field tsunami source and a probabilistic tsunami run-up distribution from tsunami run-up records. The TRRF-INV model has overcome the computational burden of tsunami forward simulations by adopting the TRRF model (Lee et al., 2020) that can rapidly estimate the alongshore tsunami run-up distribution from the earthquake fault parameters. The synthetic tests based on 1,600 scenarios have confirmed that the TRRF-INV model can provide not only reasonable estimates of tsunami source to first order but also accurate tsunami run-up distribution only with 20 run-up values with less than half a meter of uncertainty. The overall agreement on the earthquake magnitude and the epicenter of the 2014 Iquique tsunami event was satisfactory compared to the USGS report and gCMT solution, which supports the effectiveness of the TRRF-INV model. We believe that the TRRF-INV model has the potential for supporting accurate hazard assessment by providing new insights from tsunami run-up records into the tsunami source and its impact. The TRRF-INV model will be beneficial to validate the tsunami source estimated from existing tsunami inversion models, or the TRRF-INV model can serve as a starting point for constraining the tsunami source. Moreover, the TRRF-INV model can be potentially applied to estimate a tsunami source and its impact for ancient events where no data other than run-up estimates derived from sediment deposit data exists.

Appendix A: TRRF Training, Calibration, and Validation

To train the TRRF model for the northern Chile coastal region, 729 (= 3^6) tsunamigenic-earthquake scenarios were simulated. The 729 scenarios were generated in three-level factorial design (low, central, and high) of six fault parameters (LON, DIP, LEN, WID, SLP, DEP) as listed in Table 1. Note that the epicenter is the centroid of the fault. The range of the epicenter longitude LON was determined based on the historical earthquake records in the northern Chile region (Figure 1). The range of the fault length LEN, fault width WID, and slip SLP was set considering the moment magnitude (M_W = 8.2) of the 2014 Iquique earthquake.

The minimum *LEN* and the minimum *WID* were set to 90 and 40 km, respectively, considering the uncertainty (1σ) of Blaser et al. (2010)'s scaling law. The maximum *LEN* was set to 180 km based on the assumption that the uniform slip distribution is applicable up to 180 km. The maximum *WID* was limited to 90 km considering the distance between the plate boundary and the coastline. The range of the dip angle *DIP* and the depth of the top edge *DEP* were determined based on the tectonic characteristics of the northern Chile region (Comte & Suárez, 1995; Hayes et al., 2012; Shrivastava et al., 2019). In order to apply the Okal and Synolakis (2004)'s empirical formula, the strike angle (*STR*) was set parallel to the coastline, and the rake angle (*RAK*) was set to the angle that makes the strike direction perpendicular to the coastline. The epicenter latitude (*LAT*) was fixed to the near point of the city of Iquique (20°S). The initial free surface displacement was calculated using the Okada (1985)'s equations assuming an instantaneous fault rupture. The bathymetry and topography data were from the 15 arc-second data set (GEBCO Compilation Group, 2019). The bottom drag coefficient of a quadratic drag law was fixed to 10^{-4}. To reduce the computational burden, 2 h of tsunami propagation and inundation were simulated after confirming that the peak run-up values along the coastline occurred within 2 h for several synthetic earthquake scenarios. The maximum water level was interpolated bilinearly onto a regular grid (0.004° intervals). The origin was set to (20°S, 71°W), and it was used as a reference point in the Vincenty (1975)'s formula to change the coordinate system from a spherical coordinate system to a Cartesian coordinate system.

To calibrate the TRRF model, we systemically simulated two groups of scenarios. First, 75 scenarios were simulated where the fault parameters were selected as follows. We set 15 reference scenarios by randomly selecting seven fault parameters (*LAT*, *LON*, *DIP*, *LEN*, *WID*, *SLP*, *DEP*). For each reference scenario, five scenarios were generated where *STR* is 340°, 350°, 0°, 10°, and 20°, respectively, while *RAK* was fixed to 90°. Second, 100 scenarios were simulated where the fault parameters were selected as follows. We set 10 reference scenarios by randomly selecting the seven fault parameters (*LAT*, *LON*, *DIP*, *LEN*, *WID*, *SLP*, *DEP*). For each reference scenario, 10 scenarios were generated where *STR* is 340°, 350°, 0°, 10°, and 20°, respectively, while *RAK* varies from 70° to 110° at intervals of 10°. Based on the simulation results, the TRRF model was calibrated as follows:

$$\theta = \begin{cases} 0.637STR - 0.063RAK - 133.65°, & 340° \leq STR < 360° \\ 0.637STR - 0.063RAK + 95.67°, & 0° \leq STR \leq 20° \end{cases} \tag{A1}$$

$$\lambda = -0.147RAK + 103.23° \tag{A2}$$

where θ is the adjusted strike angle and λ is the adjusted rake angle, used to consider the case where the strike direction is not parallel to the coastline and/or the slip direction is not perpendicular to the coastline. More details on the calibration procedure and how the values (θ and λ) are used to estimate the tsunami run-up distribution can be found in Lee et al. (2020).

To validate the TRRF model, we simulated additional 20 scenarios where the fault parameters were randomly selected within the range in Table 1. Note that any geological background information (e.g., the earthquake recurrence interval) was not considered in random sampling. The range of six fault parameters (*LON*, *DIP*, *LEN*, *WID*, *SLP*, *DEP*) was set to the same range used in the TRRF training. The range of *LAT* was set based on the historical earthquake activities, including the 2014 Iquique earthquake. The range of *STR* was set based on the Slab model (Hayes et al., 2018). And we assumed that the *RAK* can vary 90° ± 20°. To generate scenarios similar to the 2014 Iquique earthquake, we limited the scenarios to the cases where the maximum run-up was larger than 3 m. The fault parameters of 20 scenarios are listed in Table S1. A comparison of tsunami run-up distribution between the TRRF model and the Basilisk model shows that the TRRF model can produce reliable run-up predictions (the range of *NRMSE*: 6.00%–13.92%, mean *NRMSE* = 7.90%).

Data Availability Statement

The Basilisk model used to simulate tsunamis is available at http://basilisk.fr/. The bathymetry data of the General Bathymetric Chart of the Ocean (GEBCO) is available at https://www.gebco.net/data_and_products/gridded_bathymetry_data/. The data and codes used in this paper can be accessed via repository: https://doi.org/10.17603/ds2-ej26-wa59.

References

Aki, K. (1966). Generation and propagation of G waves from the Niigata earthquake of June 16, 1964. Part 2. Estimation of earthquake moment, released energy, and stress-strain drop from the G wave spectrum. *Bulletin of the Earthquake Research Institute, University of Tokyo*, *44*(1), 73–88.

An, C., Sepúlveda, I., & Liu, P. L.-F. (2014). Tsunami source and its validation of the 2014 Iquique, Chile, earthquake. *Geophysical Research Letters*, *41*, 3988–3994. https://doi.org/10.1002/2014GL060567

Arcos, N. P., Dunbar, P. K., Stroker, K. J., & Kong, L. S. (2019). The impact of post-tsunami surveys on the NCEI/WDS global historical tsunami database. *Pure and Applied Geophysics*, *176*(7), 2809–2829. https://doi.org/10.1007/s00024-019-02191-7

Becerra, I., Aránguiz, R., González, J., & Benavente, R. (2020). An improvement of tsunami hazard analysis in Central Chile based on stochastic rupture scenarios. *Coastal Engineering Journal*, *62*(4), 473–488. https://doi.org/10.1080/21664250.2020.1812943

Blaser, L., Krüger, F., Ohrnberger, M., & Scherbaum, F. (2010). Scaling relations of earthquake source parameter estimates with special focus on subduction environment. *Bulletin of the Seismological Society of America*, *100*(6), 2914–2926. https://doi.org/10.1785/0120100111

Carvajal, M., & Gubler, A. (2016). The effects on tsunami hazard assessment in Chile of assuming earthquake scenarios with spatially uniform slip. *Pure and Applied Geophysics*, *173*(12), 3693–3702. https://doi.org/10.1007/s00024-016-1332-x

Catalán, P. A., Aránguiz, R., González, G., Tomita, T., Cienfuegos, R., González, J., et al. (2015). The 1 April 2014 Pisagua tsunami: observations and modeling. *Geophysical Research Letters*, *42*, 2918–2925. https://doi.org/10.1002/2015GL063333

Catalan, P. A., Gubler, A., Cañas, J., Zuñiga, C., Zelaya, C., Pizarro, L., et al. (2020). Design and operational implementation of the integrated tsunami forecast and warning system in Chile (SIPAT). *Coastal Engineering Journal*, *62*(3), 373–388. https://doi.org/10.1080/21664250.2020.1727402

Cesca, S., Grigoli, F., Heimann, S., Dahm, T., Kriegerowski, M., Sobiesiak, M., & Olcay, M. (2016). The Mw 8.1 2014 Iquique, Chile, seismic sequence: A tale of foreshocks and aftershocks. *Geophysical Journal International*, *204*(3), 1766–1780. https://doi.org/10.1093/gji/ggv544

Chen, K., Babeyko, A., Hoechner, A., & Ge, M. (2016). Comparing source inversion techniques for GPS-based local tsunami forecasting: A case study for the April 2014 M8.1 Iquique, Chile, earthquake. *Geophysical Research Letters*, *43*, 3186–3192. https://doi.org/10.1002/2016GL068042

Chlieh, M., Perfettini, H., Tavera, H., Avouac, J.-P., Remy, D., Nocquet, J.-M., et al. (2011). Interseismic coupling and seismic potential along the Central Andes subduction zone. *Journal of Geophysical Research*, *116*(B12). https://doi.org/10.1029/2010JB008166

Comte, D., & Suárez, G. (1995). Stress distribution and geometry of the subducting Nazca plate in northern Chile using teleseismically recorded earthquakes. *Geophysical Journal International*, *122*(2), 419–440. https://doi.org/10.1111/j.1365-246X.1995.tb07005.x

Ekström, G., Nettles, M., & Dziewonski, A. (2012). The global CMT project 2004–2010: Centroid-moment tensors for 13,017 earthquakes. *Physics of the Earth and Planetary Interiors*, *200*, 1–9. https://doi.org/10.1016/j.pepi.2012.04.002

Fuentes, M., Riquelme, S., Hayes, G., Medina, M., Melgar, D., Vargas, G., & Villalobos, A. (2016). A study of the 2015 M_w 8.3 Illapel earthquake and tsunami: Numerical and analytical approaches. *Pure and Applied Geophysics*, *173*(6), 1847–1858. https://doi.org/10.1007/s00024-016-1305-0

GEBCO Compilation Group. (2019). *Gebco 2019 grid*. https://doi.org/10.5285/836f016a-33be-6ddc-e053-6c86abc0788e

Geist, E. L., & Dmowska, R. (1999). Local tsunamis and distributed slip at the source. *Pure and Applied Geophysics*, *154*(3), 485–512. https://doi.org/10.1007/s000240050241

González, J., González, G., Aránguiz, R., Melgar, D., Zamora, N., Shrivastava, M. N., et al. (2020). A hybrid deterministic and stochastic approach for tsunami hazard assessment in Iquique, Chile. *Natural Hazards*, *100*(1), 231–254. https://doi.org/10.1007/s11069-019-03809-8

Gusman, A. R., Murotani, S., Satake, K., Heidarzadeh, M., Gunawan, E., Watada, S., & Schurr, B. (2015). Fault slip distribution of the 2014 Iquique, Chile, earthquake estimated from ocean-wide tsunami waveforms and GPS data. *Geophysical Research Letters*, *42*, 1053–1060. https://doi.org/10.1002/2014GL062604

Hanks, T. C., & Kanamori, H. (1979). A moment magnitude scale. *Journal of Geophysical Research*, *84*(B5), 2348–2350. https://doi.org/10.1029/JB084iB05p02348

Hayes, G. P., Herman, M. W., Barnhart, W. D., Furlong, K. P., Riquelme, S., Benz, H. M., et al. (2014). Continuing megathrust earthquake potential in Chile after the 2014 Iquique earthquake. *Nature*, *512*(7514), 295–298. https://doi.org/10.1038/nature13677

Hayes, G. P., Moore, G. L., Portner, D. E., Hearne, M., Flamme, H., Furtney, M., & Smoczyk, G. M. (2018). Slab2, a comprehensive subduction zone geometry model. *Science*, *362*(6410), 58–61. https://doi.org/10.1126/science.aat4723

Hayes, G. P., Wald, D. J., & Johnson, R. L. (2012). Slab1.0: A three-dimensional model of global subduction zone geometries. *Journal of Geophysical Research*, *117*(B1). https://doi.org/10.1029/2011JB008524

Ho, T.-C., Satake, K., Watada, S., & Fujii, Y. (2019). Source estimate for the 1960 Chile earthquake from joint inversion of geodetic and transoceanic tsunami data. *Journal of Geophysical Research: Solid Earth*, *124*, 2812–2828. https://doi.org/10.1029/2018JB016996

Hoshiba, M., & Ozaki, T. (2014). Earthquake early warning and tsunami warning of the Japan Meteorological Agency, and their performance in the 2011 off the Pacific coast of Tohoku Earthquake (M_w 9.0). In F. Wenzel, & J. Zschau (Eds.), Early warning for geological disasters: Scientific methods and current practice (pp. 1–28). Springer Berlin Heidelberg. https://doi.org/10.1007/978-3-642-12233-0-1

Ioki, K., & Tanioka, Y. (2016). Re-estimated fault model of the 17th century great earthquake off Hokkaido using tsunami deposit data. *Earth and Planetary Science Letters*, *433*, 133–138. https://doi.org/10.1016/j.epsl.2015.10.009

Kulikov, E. A., Rabinovich, A. B., & Thomson, R. E. (2005). Estimation of tsunami risk for the coasts of Peru and northern Chile. *Natural Hazards*, *35*(2), 185–209. https://doi.org/10.1007/s11069-004-4809-3

Lay, T., Ammon, C. J., Kanamori, H., Xue, L., & Kim, M. J. (2011). Possible large near-trench slip during the 2011 M_w 9.0 off the Pacific coast of Tohoku Earthquake. *Earth Planets and Space*, *63*(7), 32. https://doi.org/10.5047/eps.2011.05.033

Lay, T., Yue, H., Brodsky, E. E., & An, C. (2014). The 1 April 2014 Iquique, Chile, M_w 8.1 earthquake rupture sequence. *Geophysical Research Letters*, *41*, 3818–3825. https://doi.org/10.1002/2014GL060238

Lee, J.-W., Irish, J. L., & Weiss, R. (2020). Rapid prediction of alongshore run-up distribution from near-field tsunamis. *Natural Hazards*, *104*(2), 1157–1180. https://doi.org/10.1007/s11069-020-04209-z

MacInnes, B. T., Weiss, R., Bourgeois, J., & Pinegina, T. K. (2010). Slip distribution of the 1952 Kamchatka Great Earthquake based on near-field tsunami deposits and historical records. *Bulletin of the Seismological Society of America*, *100*(4), 1695–1709. https://doi.org/10.1785/0120090376

Mandli, K. T., Ahmadia, A. J., Berger, M., Calhoun, D., George, D. L., Hadjimichael, Y., et al. (2016). Clawpack: Building an open source ecosystem for solving hyperbolic PDEs. *PeerJ Computer Science*, *2*, e68. https://doi.org/10.7717/peerj-cs.68

Martin, M. E., Weiss, R., Bourgeois, J., Pinegina, T. K., Houston, H., & Titov, V. V. (2008). Combining constraints from tsunami modeling and sedimentology to untangle the 1969 Ozernoi and 1971 Kamchatskii tsunamis. *Geophysical Research Letters*, *35*. https://doi.org/10.1029/2007GL032349

Melgar, D., Williamson, A. L., & Salazar-Monroy, E. F. (2019). Differences between heterogenous and homogenous slip in regional tsunami hazards modelling. *Geophysical Journal International*, *219*(1), 553–562. https://doi.org/10.1093/gji/ggz299

Muhammad, A., & Goda, K. (2018). Impact of earthquake source complexity and land elevation data resolution on tsunami hazard assessment and fatality estimation. *Computers & Geosciences*, *112*, 83–100. https://doi.org/10.1016/j.cageo.2017.12.009

Nanayama, F., Satake, K., Furukawa, R., Shimokawa, K., Atwater, B. F., Shigeno, K., & Yamaki, S. (2003). Unusually large earthquakes inferred from tsunami deposits along the Kuril trench. *Nature*, *424*(6949), 660–663. https://doi.org/10.1038/nature01864

Okada, Y. (1985). Surface deformation due to shear and tensile faults in a half-space. *Bulletin of the Seismological Society of America*, *75*(4), 1135–1154.

Okal, E. A., & Synolakis, C. E. (2004). Source discriminants for near-field tsunamis. *Geophysical Journal International*, *158*(3), 899–912. https://doi.org/10.1111/j.1365-246X.2004.02347.x

Piatanesi, A., Tinti, S., & Gavagni, I. (1996). The slip distribution of the 1992 Nicaragua Earthquake from tsunami run-up data. *Geophysical Research Letters*, *23*(1), 37–40. https://doi.org/10.1029/95GL03606

Popinet, S. (2015). A quadtree-adaptive multigrid solver for the Serre–Green–Naghdi equations. *Journal of Computational Physics*, *302*, 336–358. https://doi.org/10.1016/j.jcp.2015.09.009

Ragon, T., Sladen, A., & Simons, M. (2018). Accounting for uncertain fault geometry in earthquake source inversions – I: Theory and simplified application. *Geophysical Journal International*, *214*(2), 1174–1190. https://doi.org/10.1093/gji/ggy187

Romano, F., Piatanesi, A., Lorito, S., Tolomei, C., Atzori, S., & Murphy, S. (2016). Optimal time alignment of tide-gauge tsunami waveforms in nonlinear inversions: Application to the 2015 Illapel (Chile) earthquake. *Geophysical Research Letters*, *43*, 11–226. https://doi.org/10.1002/2016GL071310

Ruiz, J., Fuentes, M., Riquelme, S., Campos, J., & Cisternas, A. (2015). Numerical simulation of tsunami runup in northern Chile based on non-uniform k^{-2} slip distributions. *Natural Hazards*, *79*(2), 1177–1198. https://doi.org/10.1007/s11069-015-1901-9

Satake, K. (1987). Inversion of tsunami waveforms for the estimation of a fault heterogeneity: Method and numerical experiments. *Journal of Physics of the Earth*, *35*(3), 241–254. https://doi.org/10.4294/jpe1952.35.241

Satake, K. (2009). Tsunamis, inverse problem of. In R. A. Meyers (Ed.), Encyclopedia of complexity and systems science (pp. 9631–9644). Springer New York. https://doi.org/10.1007/978-0-387-30440-3_570

Schurr, B., Asch, G., Hainzl, S., Bedford, J., Hoechner, A., Palo, M., et al. (2014). Gradual unlocking of plate boundary controlled initiation of the 2014 Iquique earthquake. *Nature*, *512*(7514), 299–302. https://doi.org/10.1038/nature13681

Sepúlveda, I., Liu, P. L.-F., Grigoriu, M., & Pritchard, M. (2017). Tsunami hazard assessments with consideration of uncertain earthquake slip distribution and location. *Journal of Geophysical Research: Solid Earth*, *122*, 7252–7271. https://doi.org/10.1002/2017JB014430

Shrivastava, M. N., González, G., Moreno, M., Soto, H., Schurr, B., Salazar, P., & Báez, J. C. (2019). Earthquake segmentation in northern Chile correlates with curved plate geometry. *Scientific Reports*, *9*(1), 1–10. https://doi.org/10.1038/s41598-019-40282-6

Synolakis, C., & Okal, E. (2005). 1992–2002: Perspective on a decade of post-tsunami surveys. In K. Satake (Ed.), Tsunamis: Case studies and recent developments (pp. 1–29). Springer Netherlands. https://doi.org/10.1007/1-4020-3331-1_1

Vincenty, T. (1975). Direct and inverse solutions of geodesics on the ellipsoid with application of nested equations. *Survey Review*, *23*(176), 88–93. https://doi.org/10.1179/sre.1975.23.176.88

Williamson, A., Newman, A., & Cummins, P. (2017). Reconstruction of coseismic slip from the 2015 Illapel earthquake using combined geodetic and tsunami waveform data. *Journal of Geophysical Research: Solid Earth*, *122*, 2119–2130. https://doi.org/10.1002/2016JB013883

Yokota, Y., Koketsu, K., Fujii, Y., Satake, K., Sakai, S., Shinohara, M., & Kanazawa, T. (2011). Joint inversion of strong motion, teleseismic, geodetic, and tsunami datasets for the rupture process of the 2011 Tohoku earthquake. *Geophysical Research Letters*, *38*. https://doi.org/10.1029/2011GL050098

Yue, H., Lay, T., Rivera, L., An, C., Vigny, C., Tong, X., & Báez Soto, J. C. (2014). Localized fault slip to the trench in the 2010 Maule, Chile M_w = 8.8 earthquake from joint inversion of high-rate GPS, teleseismic body waves, InSAR, campaign GPS, and tsunami observations. *Journal of Geophysical Research: Solid Earth*, *119*, 7786–7804. https://doi.org/10.1002/2014JB011340

Zhou, T., Meng, L., Xie, Y., & Han, J. (2019). An adjoint-state full-waveform tsunami source inversion method and its application to the 2014 Chile-Iquique tsunami event. *Journal of Geophysical Research: Solid Earth*, *124*, 6737–6750. https://doi.org/10.1029/2018JB016678